Unveiling the Impact of Impurity Phases on the Electrochemical Performance of Cobalt-Free Analogs of (Mg$_{0.2}$Co$_{0.2}$Ni$_{0.2}$Cu$_{0.2}$Zn$_{0.2}$)O as anode for Lithium-ion Batteries

Modeste N. Tegomoh[1] and Anne C. Co[1]

[1]Department of Chemistry and Biochemistry, The Ohio State University, Columbus, OH 43210, USA.

Micrometer-size particles of the pure single-phase rock salt multi-metals oxide, (Mg$_{0.2}$Co$_{0.2}$Ni$_{0.2}$Cu$_{0.2}$Zn$_{0.2}$)O, have demonstrated long-term cycling stability and excellent rate performance as an anode for lithium-ion batteries. Such a feat has only been achieved with the nanostructuring of binary transition metal oxides. This success has led to the preparation of several pure single-phase spinel multi-metal oxides with significantly higher capacities. A common belief regarding these complex oxides is that the pure single-phase is a prerequisite for their outstanding electrochemical performance. Deviation from a pure single-phase is thought to harm their electrochemical performance. Here, we prepare and characterize the cobalt-free analogs of (Mg$_{0.2}$Co$_{0.2}$Ni$_{0.2}$Cu$_{0.2}$Zn$_{0.2}$)O using a traditional solid-state synthesis method by replacing cobalt with iron and manganese to give (Mg$_{0.2}$Fe$_{0.2}$Ni$_{0.2}$Cu$_{0.2}$Zn$_{0.2}$)O and (Mg$_{0.2}$Mn$_{0.2}$Ni$_{0.2}$Cu$_{0.2}$Zn$_{0.2}$)O respectively. These analogs were prepared in an air and an argon atmosphere to yield several compositions with different mixtures of crystalline secondary phases. The electrochemical performance of the pure single-phase (Mg$_{0.2}$Co$_{0.2}$Ni$_{0.2}$Cu$_{0.2}$Zn$_{0.2}$)O is used as a benchmark to compare the performance of the cobalt-free multi-phase analogs. The results indicate that although these cobalt-free analogs are not pure single-phase materials, their electrochemical performance is similar to that observed with (Mg$_{0.2}$Co$_{0.2}$Ni$_{0.2}$Cu$_{0.2}$Zn$_{0.2}$)O, suggesting that a pure single-phase might not be a prerequisite for an excellent electrochemical performance for these complex multi-metal oxides.

I.

Since the discovery that transition metal oxides can reversibly store lithium through a reaction mechanism termed conversion-type reaction[1], extensive research has been reported on metal salts, oxides, and their derivative compounds. This interest is largely due to their high storage capacity, enabled by multiple-electron transfers when these materials are used as electrodes[2-9]. However, some of these materials experience significant capacity fade and low power density, particularly when the particles are at the micrometer scale[1,10,11].

In 2015, Rost *et al*. (ref.[12]) introduced a compositionally complex rock salt oxide (Mg$_{0.2}$Co$_{0.2}$Ni$_{0.2}$Cu$_{0.2}$Zn$_{0.2}$)O. The compound's micrometer-sized particle distribution has demonstrated long-term cycling stability when used as an anode in lithium-ion batteries[13,14] (LIBs). This contrasts with the typical need for nanostructuring in individual

binary transition metal oxides to attain similar stability and performance levels[15,16]. This material also exhibits characteristics suitable for high-power applications in LIBs, with a capacity reaching about 400 mAh g^{-1} at a current density of 3 A g^{-1} (ref.[13,14]). An intensive investigation of the lithium storage mechanism in this compound has been conducted using various analytical techniques. These studies aim to identify the factors contributing to its exceptional electrochemical performance compared to individual binary transition metal oxides[13,14,17,18].

The metal ions in this pure single-phase rock salt material are all in a +2 oxidation state and thus can provide a maximum of two electrons per formula unit. The single Wycoff site available for the metals in the rock salt structure offers no direct way to improve the capacity of this material. Consequently, several related structures have been investigated, such as the spinel $(Co_{0.2}Mn_{0.2}V_{0.2}Fe_{0.2}Zn_{0.2})_3O_4$, where the transition metal can exhibit multiple oxidations states: Co in +2 and +3, Mn in +2 and +4, V in +5, Fe in +2 and +3, and Zn in +2 (ref. [19]). The variable oxidation state of these metals enables an outstanding capacity of approximately 900 mAh g^{-1} at a current density of 0.2 A g^{-1}. Additionally, a series of single-phase spinels have been reported with similarly excellent electrochemical performance, including $(Mg_{0.2}Cr_{0.2}Mn_{0.2}Fe_{0.2}Co_{0.2})O$ (ref.[20]), $(Cr_{0.2}Mn_{0.2}Fe_{0.2}Co_{0.2}Ni_{0.2})O$ (ref.[20]), $(FeCoNiCrMnXLi)_3O_4$ (X = Cu, Mg, Zn) (ref.[21]), $(TiFeCoNiZn)_3O_4$ (ref.[22]), and $(Mg_{0.2}Ti_{0.2}Zn_{0.2}Cu_{0.2}Fe_{0.2})O$ (ref.[23]). A common feature among these materials is that they are all pure single-phase crystalline compounds, with no additional secondary phases present. This observation, along with the study by Patra *et al.* (ref.[24]), which demonstrates the negative effect of secondary phases on the electrochemical performance of these complex oxides, suggests that maintaining a pure single-phase crystalline structure is crucial for achieving the outstanding electrochemistry observed in these multi-metal complex oxides. However, a recent study by Nguyen *et al.* (ref.[25]) indicates that a well-tailored secondary phase might enhance these complex oxides' electrochemical properties, suggesting a potential area for further exploration.

In this study, analogs of $(Mg_{0.2}Co_{0.2}Ni_{0.2}Cu_{0.2}Zn_{0.2})O$ were synthesized using a traditional solid-state method by replacing Co with Fe and Mn to form $(Mg_{0.2}Fe_{0.2}Ni_{0.2}Cu_{0.2}Zn_{0.2})O$ and $(Mg_{0.2}Mn_{0.2}Ni_{0.2}Cu_{0.2}Zn_{0.2})O$, respectively. To our knowledge, there are no previous reports on the preparation of these compounds. A plausible reason for this could be the difficulty in obtaining a pure single-phase material using the synthesis methods applied in this work. These materials were prepared in air and an argon atmosphere, resulting in compositions with different crystalline secondary phases. The compositions containing Fe and Mn, prepared in air and argon, are referred to as Fe-air, Fe-argon, and Mn-air, Mn-argon, respectively. The electrochemical performance of the pure single-phase $(Mg_{0.2}Co_{0.2}Ni_{0.2}Cu_{0.2}Zn_{0.2})O$ serves as a benchmark for comparison with these samples. The results indicate that, despite Fe-air, Fe-argon, Mn-air, and Mn-argon not being pure single-phase materials, their electrochemical performance is similar to that of $(Mg_{0.2}Co_{0.2}Ni_{0.2}Cu_{0.2}Zn_{0.2})O$. This suggests that a pure single-phase structure is not necessarily a prerequisite for good electrochemical performance in these complex multi-metal oxides.

https://doi.org/10.26434/chemrxiv-2024-mdldd **ORCID:** https://orcid.org/0000-0002-4275-1860 Content not peer-reviewed by ChemRxiv. **License:** CC BY-NC-ND 4.0

II.   **Methods:**

Synthesis. All materials presented in this work were prepared using a traditional solid-state method. The precursors used included NiO (Sigma Aldrich, 99.9%), CuO (Sigma Aldrich, 99.9%), ZnO (Alfa Aesar, 99.9%), MgO (Sigma Aldrich, 99.9%), CoO (Alfa Aesar, 99.99%), MnO (Aesar, 99.9%), and FeO (Sigma Aldrich, 99.9%). Equimolar amounts of these precursors were thoroughly mixed in an agate mortar, pelletized (with each pellet containing about 0.5 g of mixed material), and then heated in air (for $(Mg_{0.2}Co_{0.2}Ni_{0.2}Cu_{0.2}Zn_{0.2})O$, Fe-air, and Mn-air) or an argon atmosphere (for Fe-argon and Mn-argon) using a Lindberg Tube Furnace in a quartz glass boat at 1100 ^oC for 20 h. The red-hot pellets were quenched based on the environment. For the air samples, the pellets were rapidly transferred onto a copper plate to quench in air, while for the argon samples, the pellets were moved toward the argon gas inlet immediately after increasing the gas flow, quenching them in an argon atmosphere. The cooled pellets were then ground into a powder using an agate mortar. To further reduce the particle size, the ground powder was ball-milled in air for 3 h using a Deco-PBM-V-0.4L vertical lab planetary ball miller (Hanchen Instrument), with alumina as the milling media and a 3:1 ball (3 mm diameter) to powder ratio.

Electrode preparation. Slurries composed of 65%, 25%, and 10% by weight of the ball-milled active material, carbon black (Carbon Vulcan Black XC-72R), and polyvinylidene fluoride (PVDF, MTI Corp.), respectively, were prepared using N-methyl-2-pyrrolidone (NMP, MTI Corp.) as a solvent. The slurry was cast onto a thin copper foil (9 μm, MTI Corp.) current collector using an adjustable doctor blade (MSK-AFA I, MTI CORP.). The coated foil was then dried at 65 ^oC in air for 4 h, followed by overnight drying at 100 ^oC under vacuum to completely remove any residual solvent. A 1 M solution of lithium hexafluorophosphate ($LiPF_6$) in a 1:1 weight ratio of ethylene carbonate (EC) and dimethyl carbonate (DMC) was used as the electrolyte (Purolyte A5 Series, Novolyte Technologies). Coin-type cells were assembled with 400 μm thick Li metal foil (Alfa Aesar, 99.9%) and glass microfiber separator (Sigma Aldrich, Whatman GF/A) inside an argon-filled glovebox (mBraun, $[O_2] < 0.5$ ppm, $[H_2O] < 0.5$ ppm).

Electrochemical characterization. Galvanostatic charge/discharge measurements were performed at room temperature using a battery testing system 8.0 (Neware). Cyclic voltammogram (CV) measurements were conducted at room temperature using a VMP3 multichannel potentiostat (BioLogic). All capacity measurements were normalized to the mass of the active material, with the electrode loading density being approximately 1-2 mg cm^{-2}.

Materials characterization. Powder X-ray diffraction (XRD) patterns were collected using a Bruker D8 Advanced diffractometer with a copper K_α radiation and a LYNXEYE detector having a fixed divergence slit (0.3^o). Scanning electron microscopy (SEM) and energy-dispersive X-ray spectroscopy (EDS) images were obtained using a Thermo Scientific Apreo field-emission scanning electron microscope at the Center for Electron Microscopy and Analysis (CEMAS) at The Ohio State University (OSU).

3

III.   Results and Discussion

1.   Structural characterization

1.1. $(Mg_{0.2}Fe_{0.2}Ni_{0.2}Cu_{0.2}Zn_{0.2})O$ samples

$(Mg_{0.2}Fe_{0.2}Ni_{0.2}Cu_{0.2}Zn_{0.2})O$-Ar. All materials presented in this work were prepared using a traditional solid-state method. The crystallinity of the materials was investigated using a powder X-ray diffractometer (XRD). The powder XRD pattern of the as-prepared Fe-argon material (bottom panel of Fig. 1A) shows a multi-phase crystalline mixture, which remains after ball-milling (top panel of Fig. 1A). Scanning electron microscopy (SEM) analysis of the as-prepared Fe-argon material (bottom image of Fig. 1A) shows a wide range of particle size distribution, approximately 2-10 μm. Ball-milling reduced the particle to an approximate range of 0.5-1.0 μm (top image of Fig. 1A). SEM combined with energy-dispersive x-ray spectroscopy (SEM/EDS) provided insight into the elemental distribution within this complex mixture. Figure 1C shows the SEM/EDS mapping of the ball-milled Fe-argon sample, illustrating the segregation of iron and copper elements. The powder XRD analysis of the Fe-argon material can be indexed to three distinct cubic phases with point groups Pn-3m, Fm-3m, and Fd-3m. The lattice constant of the Pn-3m cubic phase matches well with the copper(I) oxide reference, while the spinel phase lattice constant aligns with the Fe_3O_4 reference. SEM/EDS mapping was obtained to investigate these observations further, and Figure 1C clearly shows that iron and copper are segregated into clusters in the EDS mapping images. Since oxygen is homogeneously distributed throughout the sample, it can be concluded that all three crystalline phases are oxide compounds. Zinc, nickel, and magnesium exhibit similar distribution patterns, leading to the assignment of the unlabeled rock salt phase in the powder XRD (bottom panel of Fig. 1A) as an oxide compound composed predominantly of Zn, Ni, and Mg.

The distinct iron and copper distribution patterns in the EDS mapping support the identification that the Pn-3m cubic phase is copper(I) oxide, and the spinel phase is Fe_3O_4. It is expected that a redox-sensitive species such as Fe^{2+}, present in the form of FeO, would be oxidized to a more stable form, such as Fe_3O_4, in the presence of Cu^{2+} under extreme conditions of 1100 °C used in this study. However, Balcerzak *et al.* (ref.[26]) have demonstrated the formation of $(Mg_{0.2}Co_{0.2}Ni_{0.2}Cu_{0.2}Zn_{0.2})O$ using the spinel Co_3O_4 as the cobalt source rather than CoO. In this work, it is thus surprising that the spinel Fe_3O_4 does not form a solid solution with the rock salt phase. The preparation of $(Mg_{0.2}Co_{0.2}Ni_{0.2}Cu_{0.2}Zn_{0.2})O$ under argon at 1100 °C was attempted, and the XRD shows a multi-phase crystalline mixture containing a rock salt phase and the cubic Pn-3m phase (Fig. S1). This Pn-3m phase is copper(I) oxide, as previously identified, and its presence indicates the reduction of copper(II) oxide by a redux-sensitive cation. The most likely redux-sensitive species among the other cations in this compound is Co^{2+} (from CoO),

4

which can easily be oxidized to the spinel Co_3O_4. However, no spinel phase is identified in the XRD pattern (Fig. S1), consistent with Balcerzak *et al.* (ref.[26]). FeO shows all the hallmarks of CoO, from structure properties (see Table S1) to the thermochemistry as demonstrated, but fails to form a solid solution in the Fe-argon system as opposed to CoO in the $(Mg_{0.2}Co_{0.2}Ni_{0.2}Cu_{0.2}Zn_{0.2})O$ system.

$(Mg_{0.2}Fe_{0.2}Ni_{0.2}Cu_{0.2}Zn_{0.2})O$-air. $(Mg_{0.2}Fe_{0.2}Ni_{0.2}Cu_{0.2}Zn_{0.2})O$ was prepared in air, and the powder XRD pattern of the as-synthesized material (bottom panel of Fig. 1B) also shows a multi-phase crystalline mixture, which is conserved after ball-milling (top panel of Fig. 1B). SEM analysis for the as-synthesized Fe-air material (bottom image of Fig. 1B) shows a wide range of particle size distribution, reaching about 2-15 μm. This particle size was reduced via ball-milling to an approximate range of about 0.5-1.0 μm (top image of Fig. 1B). Figure 1D shows the SEM/EDS mapping of the ball-milled Fe-air sample, where one can observe the segregation of the iron element.

The powder XRD pattern of the Fe-air sample (Fig. 1B) can be indexed to only two phases: a spinel phase and a rock salt phase. The spinel phase again matches the peaks and lattice parameter of the reference Fe_3O_4 compound, and the SEM/EDS mapping (Fig. 1D), which shows cluster spots rich in iron, is used to corroborate these findings. The remaining elements, namely copper, zinc, magnesium, and nickel, show similar EDS mapping, suggesting that the rock salt phase in the powder XRD pattern is predominantly composed of these four elements. Although the iron EDS mapping image shows some clustering, it also shows that some iron fractions are homogeneously distributed with copper, zinc, magnesium, and nickel. The composition of the rock salt phase in this sample is more likely $(Mg_{0.25}Ni_{0.25}Cu_{0.25}Zn_{0.25})_{1-x}Fe_xO$, assuming Fe is in a +2-oxidation state. It is also possible that the fraction of Fe homogeneously distributed in the EDS mapping may have originated from fine particles of Fe_3O_4 deposited on the surface of the rock salt phase since the sample was ball-milled to reduce the particle size. However, the $(Mg_{0.25}Ni_{0.25}Cu_{0.25}Zn_{0.25})_{1-x}Fe_xO$ structure is a more accurate description of this rock salt phase since the four-component rock salt phase $(Mg_{0.25}Ni_{0.25}Cu_{0.25}Zn_{0.25})O$ shows severe structural distortion (bottom panel of Fig. S2) which has been ascribed to a tetragonal distortion caused by the Jahn-Teller effect initiated by the Cu^{2+} ion in the stucture[3]. This distortion does not manifest on the rock salt phase in the XRD in Figure 1B (bottom panel). It is, therefore, possible to prepare a single-phase rock salt $(Mg_{0.25}Ni_{0.25}Cu_{0.25}Zn_{0.25})_{1-x}Fe_xO$ by simply controlling the number of moles of FeO added before heating in air. Eventually, it would also be interesting to investigate the magnetic properties of this Fe-doped complex oxide system.

Another approach was attempted to synthesize a single-phase $(Mg_{0.2}Fe_{0.2}Ni_{0.2}Cu_{0.2}Zn_{0.2})O$ compound using a solid-state method, where a premade single-phase $(Mg_{0.25}Ni_{0.25}Cu_{0.25}Zn_{0.25})O$ was ball milled with FeO (0.25 moles of FeO for every mole of $(Mg_{0.25}Ni_{0.25}Cu_{0.25}Zn_{0.25})O$) and the powder XRD of the mixture was measured

(middle panel of Fig. S2). It is clear from the XRD that the two materials are still present as separate phases after ball milling. The mixture was then placed in a preheated tube furnace at 1100 °C in an argon atmosphere for 20 hours and quenched in argon. The resulting material (top panel of Fig. S2) gave an XRD pattern identical to that observed with the Fe-Argon.
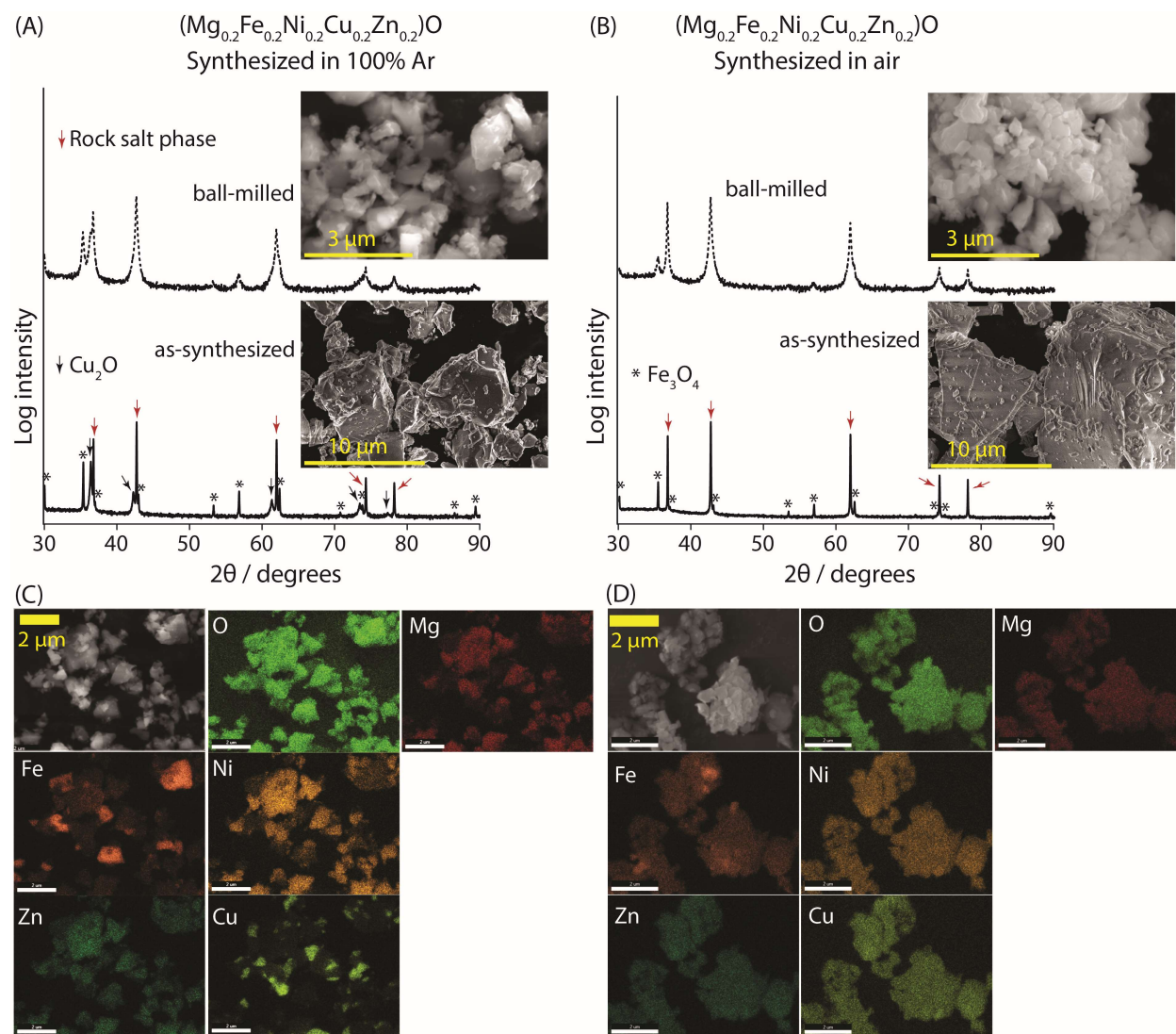

Figure 1. Characterization of $(Mg_{0.2}Fe_{0.2}Ni_{0.2}Cu_{0.2}Zn_{0.2})O$ prepared in an argon or air atmosphere. (A) and (B) Powder XRD patterns and SEM images of the as-prepared (bottom) and ball-milled (top) argon (A) and air (B) synthesized sample. (C) and (D) SEM/EDS mapping of the elemental distribution obtained for the ball-milled sample of the argon (C) and air (D) samples.

6

1.2. $(Mg_{0.2}Mn_{0.2}Ni_{0.2}Cu_{0.2}Zn_{0.2})O$ sample

$(Mg_{0.2}Mn_{0.2}Ni_{0.2}Cu_{0.2}Zn_{0.2})O$-argon. The series of experiments that were previously conducted with iron were repeated here by substituting iron with manganese. The powder XRD pattern of the as-prepared Mn-argon material (bottom panel of Fig. 2A) shows a single-phase crystalline material, which is retained after ball-milling (top panel of Fig. 2A). SEM analysis for the as-prepared Mn-argon material (bottom image of Fig. 2A) shows a regular particles morphology and a wide range of particle size distribution, reaching about 2-10 μm. This particle size was further reduced via ball-milling to an approximate range of about 0.5-3.0 μm (top image of Fig. 2A). SEM/EDS was used to gain more insight into the elemental distribution in this seemingly single-phase rock salt material. Figure 2C shows the SEM/EDS mapping of the ball-milled Mn-argon sample, showing the segregation of the copper element.

The powder XRD of the Mn-argon sample (Fig. 2A) shows a single-phase crystalline pattern that can be indexed to a rock salt phase. However, EDS mapping (Fig. 2C) shows that while Mg, Ni, Mn, and Zn are homogenously distributed across the material, Cu seems to be segregated from the four elements resulting in Cu-rich and Cu-deficient regions. An interesting finding with this EDS mapping is the distribution of the oxygen element, which appears to show some deficiency in the particles or areas rich in copper. Since oxygen is not entirely absent from these copper-rich areas, it is hypothesized that the copper-rich regions may be composed of Cu_2O. The cubic phase Cu_2O coincidentally has a lattice parameter that matches the as-synthesized Mn-argon rock salt in the bottom panel of Figure 2A. However, while the lattice constant of Cu_2O overlaps with the rock salt pattern, the intensity of the peaks does not reflect those of Cu_2O. A typical Cu_2O would have the highest intensity in the (111) plane at about 36.47° than the (200) plane at about 42.31° in Figure 2A, which is the opposite of what is observed. One plausible explanation is that the XRD pattern reflects a mixture of two cubic crystalline phases, where the cubic Cu_2O overlaps with a rock salt phase composed predominantly of Mg, Ni, Mn, Zn, and O. Finally, the lower oxygen EDS intensity in copper-rich areas is simply due to the lower content of this element in Cu_2O relative to the rock salt phase.

$(Mg_{0.2}Mn_{0.2}Ni_{0.2}Cu_{0.2}Zn_{0.2})O$-air. The $(Mg_{0.2}Mn_{0.2}Ni_{0.2}Cu_{0.2}Zn_{0.2})O$ material was also synthesized in air where the XRD reflects a multi-phase crystalline mixture (bottom panel of Fig. 2B), which is conserved after ball-milling (top panel of Fig. 2B). SEM analysis for the as-synthesized Mn-air material (bottom image of Fig. 2B) shows a wide range of particle size distribution, reaching about 2-10 μm. This particle size was reduced via ball-milling to an approximate range of about 0.5-2.0 μm (top image of Fig. 2B). Figure 2D shows the SEM/EDS mapping of the ball-milled Mn-air sample, showing the segregation of the manganese element.

The powder XRD of the Mn-air material can be indexed to two different cubic phases with point groups Fm-3m and Fd-3m. *Lin et al.* (ref.[27]) reported this spinel phase as the $CuMn_2O_4$ compound as they attempted to prepare $(MnCoNiCuZn)O_5$ using a

7

nebulized spray pyrolysis method. This phase was also observed by Chen *et al.* (ref.[28]) as they tried to prepare the manganese-doped $(MgCoNiCuZn)_{1-x}Mn_xO_5$ compound. Although the lattice parameter of this spinel phase matches well with the $CuMn_2O_4$ compound, the SEM/EDS mapping does not agree with the assignment. The EDS elemental mapping shows a segregation of the manganese and a similar distribution pattern for magnesium, nickel, and copper, while zinc is homogeneously distributed across all particles. These observations allow us to propose that the spinel phase predominantly comprises zinc and manganese, while the rock salt phase is an oxide phase consisting predominantly of magnesium, nickel, copper, and zinc. It is possible that this spinel phase can form a solid solution with the rock salt phase at a sufficiently high temperature, as demonstrated by Chen et al. (ref.[28]). However, it is beyond the scope of this work.
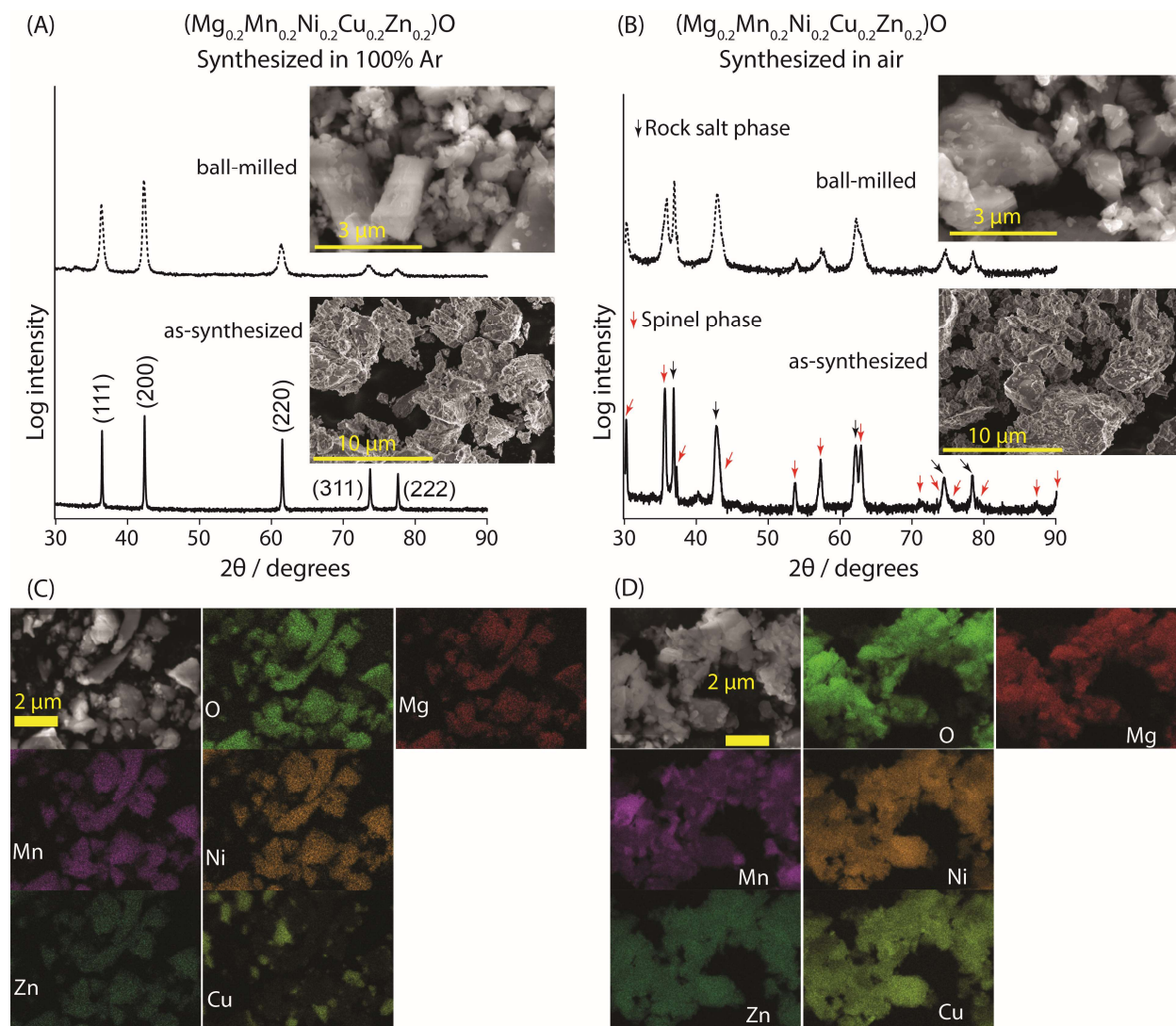
Figure 2. Characterization of (Mg$_{0.2}$Mn$_{0.2}$Ni$_{0.2}$Cu$_{0.2}$Zn$_{0.2}$)O prepared in an argon or air atmosphere. (A) and (B) Powder XRD patterns and SEM images of the as-prepared (bottom) and ball-milled (top) argon (A) and air (B) synthesized sample. (C) and (D) SEM/EDS mapping of the elemental distribution obtained for the ball-milled sample of the argon (C) and air (D) samples.
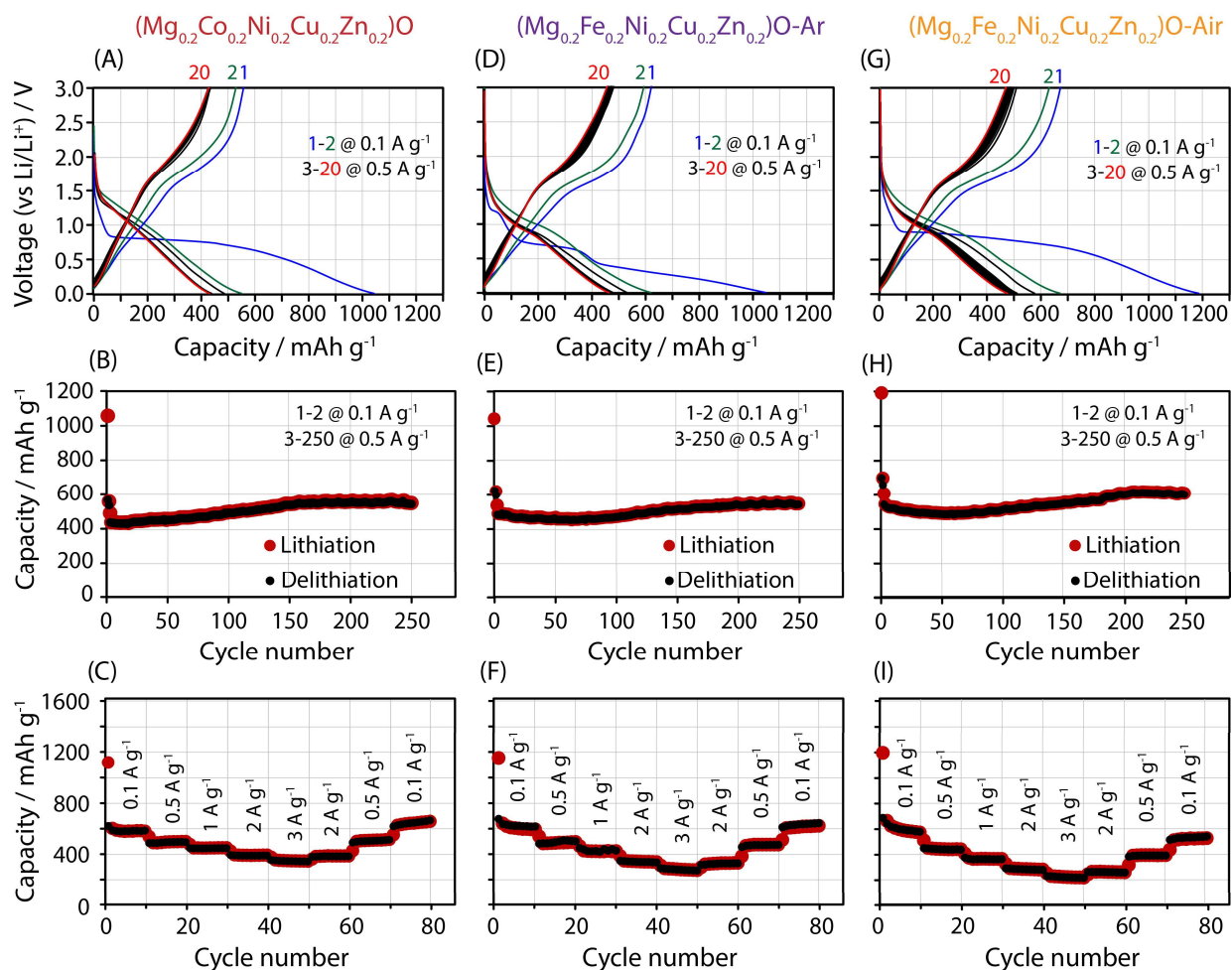
9

2.   Electrochemical Characterization

Figure 3. Electrochemical characterization of $(Mg_{0.2}Co_{0.2}Ni_{0.2}Cu_{0.2}Zn_{0.2})O$, Fe-argon, and Fe-air. (A),(D),(G) Voltage profiles for $(Mg_{0.2}Co_{0.2}Ni_{0.2}Cu_{0.2}Zn_{0.2})O$ (A), Fe-argon (D), and Fe-air (G) acquired within a voltage window of 0.01-3.00 V. (B),(E),(H) Capacity retention plots for $(Mg_{0.2}Co_{0.2}Ni_{0.2}Cu_{0.2}Zn_{0.2})O$ (B), Fe-argon (E), and Fe-air (H). The first two cycles in this voltage profile and capacity retention plots are formation cycles acquired at 100 mA g^{-1}, and the subsequent cycles are at 500 mA g^{-1}. (C),(F),(I) Rate performance of all three compounds cycled between 0.01-3.00V at 100, 500, 1000, 2000, and 3000 mA g^{-1} for $(Mg_{0.2}Co_{0.2}Ni_{0.2}Cu_{0.2}Zn_{0.2})O$ (C), Fe-argon (F), and Fe-air (I).

The electrochemical performance of $(Mg_{0.2}Co_{0.2}Ni_{0.2}Cu_{0.2}Zn_{0.2})O$, Fe-argon, Fe-air, Mn-argon, and Mn-air as an anode in LIBs was evaluated in a CR2032 coin-type battery geometry with Li-metal as the counter electrode using galvanostatic cycling. A typical loading used in this work was about 1.2 mg cm^{-2} except otherwise specified. The voltage

10

profile, capacity retention, and rate performance plots for these materials are shown in Figures 3 and 4. The first two cycles on the voltage profile and capacity retention plots are formation cycles measured within a 0.01-3.00 V voltage window and at a current density of 100 mA g^{-1}. These measurements provide a first lithiation capacity of about 1050, 1035, 1180, 1060, 1200 mAh g^{-1} and a first delithiation capacity of about 550, 610, 680, 600, 620 mAh g^{-1} for ($Mg_{0.2}Co_{0.2}Ni_{0.2}Cu_{0.2}Zn_{0.2}$)O, Fe-argon, Fe-air, Mn-argon, and Mn-air respectively. About 50% coulombic efficiency is observed for these materials on the first cycle, typical of conversion-type charge storage mechanism[1,10,11]. The long-term cycling performance was evaluated within a 0.01-3.00 V voltage range at a current density of 500 mA g^{-1}. A maximum lithiation capacity of about 570 mAh g^{-1} for ($Mg_{0.2}Co_{0.2}Ni_{0.2}Cu_{0.2}Zn_{0.2}$)O, 550 mAh g^{-1} for Fe-argon, 600 mAh g^{-1} for Fe-air, 480 mAh g^{-1} for Mn-argon, and 550 mAh g^{-1} for Mn-air was observed (Fig.3B, E, H and Fig.4E, H respectively). The long-term cycling performance of these materials shows an increase in capacity with cycling except Mn-argon, which shows a stable capacity profile over time. Figure 3A, D, G and Figure 4D, G show the voltage profile of ($Mg_{0.2}Co_{0.2}Ni_{0.2}Cu_{0.2}Zn_{0.2}$)O, Fe-argon, Fe-air, Mn-argon, and Mn-air, respectively. The first lithiation in these voltage profile plots shows a plateau at about 0.8 V for ($Mg_{0.2}Co_{0.2}Ni_{0.2}Cu_{0.2}Zn_{0.2}$)O (Fig. 3A), 0.9 V for Fe-air (Fig. 3G), 0.7 V for Mn-air (Fig. 4G) and three different plateaus at about 1.2, 0.7, 0.2 V for both Fe-argon (Fig. 3D) and Mn-argon (Fig. 4D). The subsequent cycles show a slopping voltage, quite different from the plateau observed during the first lithiation, indicative of significant structural changes in these materials after the first lithiation. Figure 3C, F, I, and Figure 4F and I show the ($Mg_{0.2}Co_{0.2}Ni_{0.2}Cu_{0.2}Zn_{0.2}$)O, Fe-argon, Fe-air, Mn-argon, and Mn-air rate performance data, respectively. These rate performance data were acquired within a voltage window of 0.01-3.00 V and with current densities of 100, 500, 1000, 2000, and 3000 mA g^{-1}. These materials demonstrate high stability at variable current densities, accumulating about 320 mAh g^{-1} for ($Mg_{0.2}Co_{0.2}Ni_{0.2}Cu_{0.2}Zn_{0.2}$)O (Fig. 3C), 280 mAh g^{-1} for Fe-argon (Fig. 3F), 220 mAh g^{-1} for Fe-air (Fig. 3I), 220 mAh g^{-1} for Mn-argon (Fig. 4F) and 210 mAh g^{-1} for Mn-air (Fig. 4I) at a current density of 3000 mA g^{-1}. The capacity of these materials fully recovers to their original values at 100 mA g^{-1} after these current cycles.
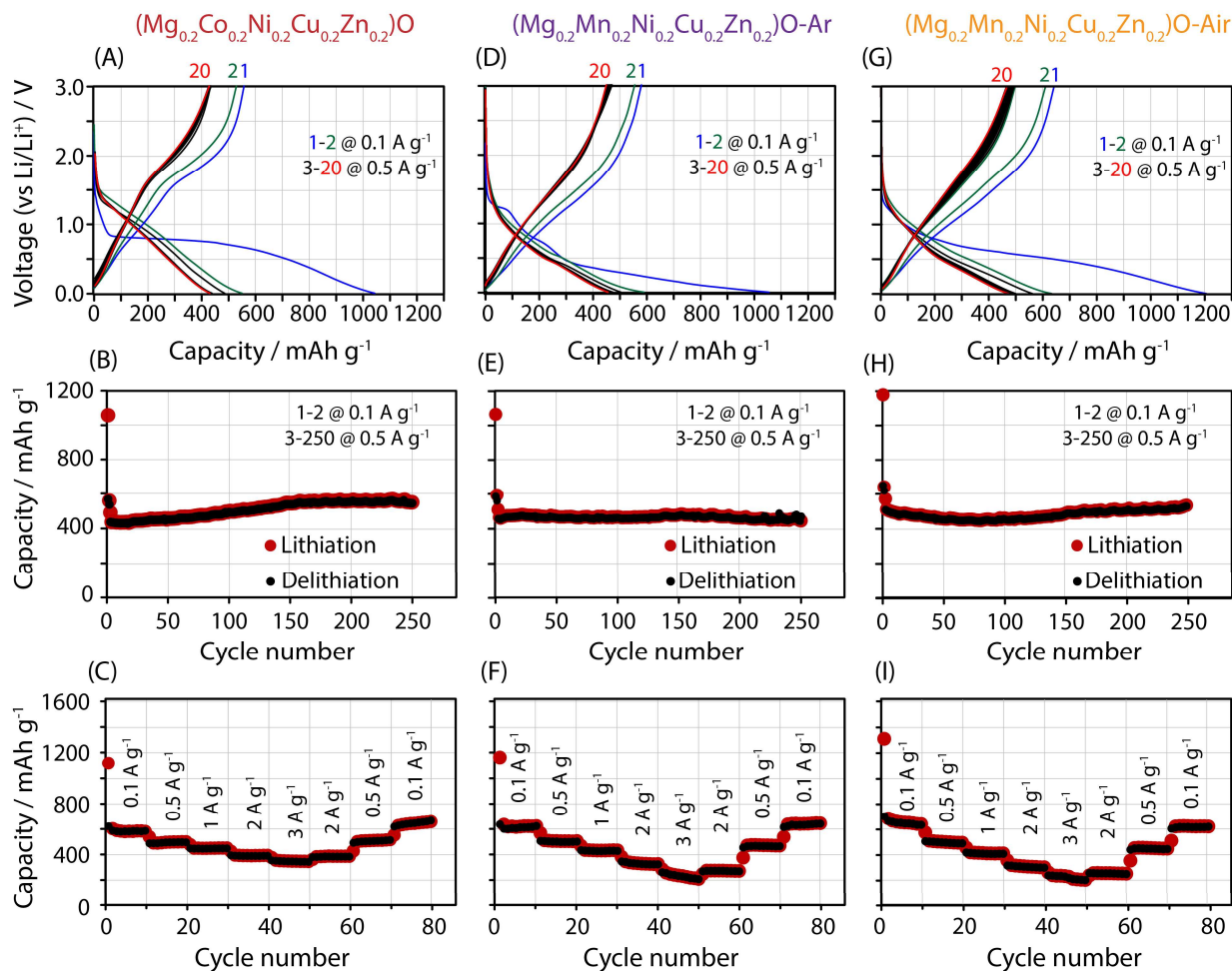
Figure 4. Electrochemical characterization of $(Mg_{0.2}Co_{0.2}Ni_{0.2}Cu_{0.2}Zn_{0.2})O$, Mn-argon, and Mn-air. (A),(D),(G) Voltage profiles for $(Mg_{0.2}Co_{0.2}Ni_{0.2}Cu_{0.2}Zn_{0.2})O$ (A), Mn-argon (D), and Mn-air (G) acquired within a voltage window of 0.01-3.00 V. (B),(E),(H) Capacity retention plots for $(Mg_{0.2}Co_{0.2}Ni_{0.2}Cu_{0.2}Zn_{0.2})O$ (B), Mn-argon (E), and Mn-air (H). The first two cycles in this voltage profile and capacity retention plots are formation cycles acquired at 100 mA g^{-1}, and the subsequent cycles are at 500 mA g^{-1}. (C),(F),(I) Rate performance of all three compounds cycled between 0.01-3.00V at 100, 500, 1000, 2000, and 3000 mA g^{-1} for $(Mg_{0.2}Co_{0.2}Ni_{0.2}Cu_{0.2}Zn_{0.2})O$ (C), Mn-argon (F), and Mn-air (I).

The electrochemical performance and lithium storage mechanism of the single-phase rock salt material, $(Mg_{0.2}Co_{0.2}Ni_{0.2}Cu_{0.2}Zn_{0.2})O$, have been extensively studied[13,14,17,18] and its electrochemical profile is used as a benchmark upon which to compare the electrochemical performance of the cobalt-free multiphase materials prepared in this work. Most multi-metal oxide compounds reported as lithium-ion anodes are pure single-phase materials. This may lead one to believe that single-phase in these materials is a prerequisite for a high-performing anode. Nguyen *et al.* (ref.[25]) recently suggested that a proper secondary phase might even be advantageous to the electrochemistry of these complex metal oxides. We considerably extended their study

by preparing analogs of the $(Mg_{0.2}Co_{0.2}Ni_{0.2}Cu_{0.2}Zn_{0.2})O$ material with a diverse mixture of secondary crystalline phases. The long-term cycling performance for the reference compound $(Mg_{0.2}Co_{0.2}Ni_{0.2}Cu_{0.2}Zn_{0.2})O$ looks similar to the multiphase analogs. They all show similar long-term capacity values, as one will expect from the number of electrons each material can store per unit formula, assuming each is a pure single-phase compound. An important thing to note regarding the long-term behavior of these materials is the exceptionally stable trend observed with the Mn-argon sample, as every other sample shows an increase in capacity over time. $(Mg_{0.2}Co_{0.2}Ni_{0.2}Cu_{0.2}Zn_{0.2})O$ does not show any visible long-term advantage over the multi-phase samples. However, it performs better at the highest current density used in this work ($3.0\ A\ g^{-1}$). The trend and the capacity values for the rate performance data look similar for all these materials except at 2.0 and $3.0\ A\ g^{-1}$, where $(Mg_{0.2}Co_{0.2}Ni_{0.2}Cu_{0.2}Zn_{0.2})O$ standouts with slightly higher capacity values. Since it has been demonstrated that the initial particle size distribution of these complex oxides can significantly affect their capacity values[9,10], it is hard to attribute these slight capacity differences at high current densities to the intrinsic property of the material.

The voltage profiles of all these materials look very similar, implying a similar mechanism of lithium storage as expected. However, the first lithiation half-cycle voltage profile looks different from sample to sample due to the difference in the initial sample composition demonstrated by the XRD and SEM/EDS mapping. For example, the Fe-argon fist lithiation half-cycle shows three different plateaus that may correspond to the three distinct phases identified on the powder XRD pattern. With this reasoning, one may ask why two plateaus are not observed on Fe-air's first lithiation voltage profile since the powder XRD shows a two-phase mixture. The spinel phase (mainly Fe_3O_4) has a first lithiation voltage of 0.9 V (ref.[29]), and the rock salt phase (mainly $(Mg_{0.25}Ni_{0.25}Cu_{0.25}Zn_{0.25})O$ has a first lithiation voltage of 0.8 V (ref.[13]). it is thus clear that the two peaks overlap to form the single plateau observed. Although the first lithiation half-cycle looks different for Fe-argon and Fe-air, their corresponding delithiation half-cycle and subsequent cycles look identical. This observation implies that, although we may initially start with different compositions for the two materials, the first lithiation eventually leads to a similar composition. The same story holds for Mn-argon and Mn-air. An exciting aspect of these multi-metal oxide materials as lithium-ion battery materials is the ease with which one can tune the voltage of a given composition by simply substituting one metal element with another or completely removing a metal component[13]. This concept is not easy to see on the voltage profiles of these materials, but it is clear on their differential capacity plots (Fig. S3 and S4). The deferential capacity plot of $(Mg_{0.2}Co_{0.2}Ni_{0.2}Cu_{0.2}Zn_{0.2})O$ shows the last delithiation peak starting at about 1.3 V and ending around 2.5 V at a current density of $100\ mA\ g^{-1}$. However, if cobalt is replaced with iron (Fe-argon and Fe-air) or Mn (Mn-argon and Mn-air), the same delithiation peak ends around 2.0 V at the same current density. That is a 0.5 V lower voltage observed for these later materials compared to the former, which, if used as an anode material in LIBs, can significantly improve energy density. To end this discussion, a ball-milled powder composed of MgO, MnO, NiO, CuO, and ZnO (Fig. S6) was used to prepare a slurry

13

similar to the ones made with the materials presented above. The electrochemical performance (Fig. S7) of these binary metal oxides mixed is not as good as the ones presented in this work. There is no doubt that these complex multi-metal oxide compounds have some exceptional electrochemistry as anode materials in LIBs. However, a pure single-phase material does not appear necessary for the outstanding electrochemistry observed.

IV.   Conclusion

The effect of secondary phases on the electrochemistry of complex multi-metal oxides such as $(Mg_{0.2}Co_{0.2}Ni_{0.2}Cu_{0.2}Zn_{0.2})O$ was investigated. The electrochemical performance of the pure single-phase $(Mg_{0.2}Co_{0.2}Ni_{0.2}Cu_{0.2}Zn_{0.2})O$ material was compared to that of the cobalt-free multi-phase Fe-air, Fe-argon, Mn-air, and Mn-argon materials and they all provided a maximum long-term capacity of about 570, 600, 550, 550, and 480 mAh g^{-1} respectively at a current density of 500 mA g^{-1} for 250 cycles. They all show similar rate performance data and voltage profile plots, suggesting that pure single-phase is not a strict requirement for the outstanding electrochemical performance observed for these complex multi-metal oxides. Since a single-phase material is not a hard constraint for good electrochemistry, as demonstrated, one is not limited by specific metal types, which gives the battery community an expanded design space without the use of critical elements such as cobalt and nickel. A less advertised advantage of these complex multi-metal compounds is the ease with which voltage can be tuned by simply substituting an element.

14

References

1. Poizot, P., Laruelle, S., Grugeon, S., Dupont, L. & Tarascon, J. M. Nano-sized transition-metal oxides as negative-electrode materials for lithium-ion batteries. *Nature* **407**, 496-499 (2000).

2. Cabana, J., Monconduit, L., Larcher, D. & Palacin, R. Beyond Intercalation-Based Li-Ion Batteries: The State of the Art and Challenges of Electrode Materials Reacting Through Conversion Reactions. *Adv. Mater*. **22**, E170-E192 (2010).

3. Reddy, M. V., Subba, G. V., Chowdari, B. R. Metal Oxides and Oxysalts as Anode Materials for Li Ion Batteries. *Chem. Rev.* **113**, 5364-5457 (2013).

4. Du, J., Li, Q., Chai, J., Jiang, L., Zhang, Q., Han, N., Zhang, W. & Tang B. Review of metal oxides as anode materials for lithium-ion batteries. *Dalton Trans.* **51**, 9584 (2022).

5. Chen, H., Qiu, N., Wu, B., Yang, Z., Sun, S. & Wang, Y. A new spinel high-entropy oxide $(Mg_{0.2}Ti_{0.2}Zn_{0.2}Cu_{0.2}Fe_{0.2})_3O_4$ with fast reaction kinetics and excellent stability as an anode material for lithium ion batteries. *RSC Adv*. **10**, 9736 (2020).

6. Courtel. F. M., Duncan, H., Abu-Lebdeh, Y. & Davidson, I. J. High capacity anode materials for Li-ion batteries based on spinel metal oxides AMn_2O_4 (A = Co, Ni, and Zn). *J. Mater. Chem.* **21**, 10206 (2011).

7. Fang, S., Bresser, D. & Passerini, S. Transition Metal Oxide Anodes for Electrochemical Energy Storage in Lithium- and Sodium-Ion Batteries. *Adv. Energy Mater*. **10**, 1902485 (2020).

8. Balaya, B. P., Li, H., Kienle, L., Maier, J. Fully reversible homogeneous and heterogeneous Li storage in RuO_2 with high capacity. *Adv. Funct. Mater*. **13**, 621-625 (2003).

9. Li, H., Balaya, P., Maier, J. Li-storage via heterogeneous reaction in selected binary metal fluorides and oxides. *J. Electrochem. Soc.* **151**, A1878-A1885 (2004).

10. Grugeon, S., Laruelle, S., Herrera-Urbina, R., Dupont, L., Poizot, P. & Tarascon, J-M. Particle Size Effects on the Electrochemical Performance of Copper Oxides toward Lithium. *Journal of the Electrochemical Society* **140** (4), A285-A292 (2001).

11. Fu, Z.-W., Huang, F., Zhang, Y., Chu, Y. & Qin, Q.-Z. The Electrochemical Reaction of Zinc Oxide Thin Films with Lithium. *J. Electrochem. Soc.* **150** (6), A714-A720 (2003).

12. Rost, C. M., Sachet, E., Borman, T., Moballegh, A., Dickey, E. C., Hou, D., Jones, J. L., Curtarolo, S. & Maria, J-P. Entropy-stabilized oxides. *Nat. Commun*. **6**, 8485 (2015).

13. Sarkar, A., Velasco, L., Wang, D., Wang, Q., Talasila, G., Biasi, L., Kubel, C., Brezesinski, T., Bhattacharya, S. S., Hahn, H. & Breitung, B. High entropy oxides for reversible energy storage. *Nat. Commun*. **9**, 3400 (2018).

14. Qiu, N., Chen, H., Yang, Z., Sun, S., Wang, Y. & Cui, Y. A high entropy oxide $(Mg_{0.2}Co_{0.2}Ni_{0.2}Cu_{0.2}Zn_{0.2})O$ with superior lithium storage performance. *Journal of Alloys and Compounds* **777**, 767-774 (2019).

15. Julian J. A. Kreissl, Jan Petit, Raika Oppermann, Pascal Cop, Tobias Gerber, *et al*. Electrochemical lithiation/delithiation of ZnO in 3D-structured electrodes: Elucidating the mechanism and the solid electrolyte interphase formation. *ACS Appl. Mater. Interfaces*, **13**, 35625-35638 (2021).

16. Mingbo Zheng, Hao Tang, Lulu Li, Qin Hu, Li Zhang, et al. Hierarchically nanostructured transition metal oxides for lithium-ion batteries. *Adv. Sci.* **5**, 1700592 (2018).

17. Ghigna, P., Airoldi, L., Fracchia, M. *et al.* Lithiation Mechanism in High-Entropy Oxides as Anode Materials for Li-Ion Batteries: An Operando XAS Study. *ACS Appl. Mater. Interfaces* **12**, 50344-50354 (2020).

18. Wang, K., Hua, W., Huang, X. *et al.* Synergy of cations in high entropy oxide lithium ion battery anode. *Nat Commun* **14**, 1487 (2023).

19. Hou, S., Su, L., Wang, S., Cui, Y., Cao, J., Min, H., Bao, J., Shen, Y., Zhang, Q., Sun, Z., Zhu, C., Chen, J., Zhang, Q., Xu, F. Unlocking the Origins of Highly Reversible Lithium Storage and Stable Cycling in a Spinel High-Entropy Oxide Anode for Lithium-Ion Batteries. *Adv. Funct. Mater.* **34**, 2307923 (2024).

20. Minouei, H., Tsvetkov, N., Kheradmandfard, M., Han, J., Kim, D.-E., Hong, S. I. Tuning the electrochemical performance of high-entropy oxide nanopowder for anode Li-ion storage via structural tailoring. *Journal of Power Sources* **549**, 232041 (2022).

21. Duan, C., Tian, K., Li, X., Wang, D., Sun, H., Zheng, R., Wang, Z., Liu, Y. New spinel high-entropy oxides $(FeCoNiCrMnXLi)_3O_4$ (X = Cu, Mg, Zn) as the anode material for lithium-ion batteries. *Ceramics International* **47**, 32025–32032 (2021).

22. Marques, O. J. B. J., Walter, M. D., Timofeeva, E. V., Segre, C. U. Effect of Initial Structure on Performance of High-Entropy Oxide Anodes for Li-Ion Batteries. *Batteries* **9**, 115 (2023).

23. Chen, H., Qiu, N., Wu, B., Yang, Z., Sun, S., Wang, Y. A new spinel high-entropy oxide $(Mg_{0.2}Ti_{0.2}Zn_{0.2}Cu_{0.2}Fe_{0.2})_3O_4$ with fast reaction kinetics and excellent stability as an anode material for lithium-ion batteries. *RSC Adv.* **10**, 9736 (2020).

24. Patra, J., Nguyen, X. T., Tsai, C.-C., Clemens, O., Li, J., Pal, P., Chan, K. W., Lee, C.-H., Chen, T. H.-Y., Ting, J.-M., Chang, J.-K. Effects of Elemental Modulation on Phase Purity and Electrochemical Properties of Co-free High-Entropy Spinel Oxide Anodes for Lithium-Ion Batteries. *Adv. Funct. Mater.* **32**, 2110992 (2022).

25. Nguyen, X. T., Patra, J., Tsai, C.-C., Xuan, W.-Y., Chen, H.-Y. T., Dyer, M. S., Clemens, O., Li, J., Majumder, S. B., Chang, J.-K., Ting, J.-M. Secondary-Phase-Induced Charge–Discharge Performance Enhancement of Co-Free High Entropy Spinel Oxide Electrodes for Li-Ion Batteries. *Adv. Funct. Mater.* **33**, 2300509 (2023).

26. Balcerzak, M., Kawamura, K., Bobrowski, R., Rutkowski, P., Brylewski, T. Mechanochemical synthesis of (Co,Cu,Mg,Ni,Zn)O high-entropy oxide and its physicochemical properties. *J. Elect. Mater.* **48**, 11 (2019).

27. Lin, L., Wang, K., Azmi, R., Wang, J., Sarkar, A., Botros, M., Najib, S., Cui, Y., Stenzel, D., Sukkurji, A. P., Wang, Q., Hahn, H., Schweidler, S., Breitung, B. Mechanochemical synthesis: route to novel rock-salt structured high-entropy oxides and oxyfluorides. *J. Mater. Sci.* **55**, 16879–16889 (2020).

28. Chen, J., Liu, W., Liu, J., Zhang, X., Yuan, M., Zhao, Y., Yan, J., Hou, M., Yan, J., Kunz, M., Tamura, N., Zhang, H., Yin, Z. Stability and Compressibility of Cation-Doped High Entropy Oxide MgCoNiCuZnO5. *J. Phys. Chem. C* **123**, 17735−17744 (2019).

29. Hariharan, S., Saravanan, K., Ramar, V., Balaya, P. A rationally designed dual role anode material for lithium-ion and sodium-ion batteries: case study of eco-friendly Fe_3O_4. *Phys.Chem. Chem. Phys.* **15**, 2945 (2013).